Nuclear Instruments and Methods in Physics Research B 575 (2026) 166112

Contents lists available at ScienceDirect

Nuclear Inst. and Methods in Physics Research, B

journal homepage: www.elsevier.com/locate/nimb

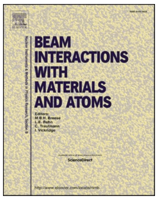

Characterization of the OctoIonGuide setup for high-resolution photoionization studies of low-charge atomic ions

Awad E.A. Mohamed [a,b,*], Marcello Coreno [b,c], Daniele Catone [b], Fabio Zuccaro [b], Stefano Orlando [b], Javad Rezvani [a], Andrea Di Cicco [a], Monica de Simone [d]

[a] *Physics Division, School of Science and Technology, Università di Camerino, 62032 Camerino, MC, Italy*
[b] *CNR - Istituto di Struttura della Materia (ISM), 00133 Roma, Italy*
[c] *Elettra-Sincrotrone Trieste, 34149 Trieste, Italy*
[d] *CNR - Istituto Officina dei Materiali (IOM), 34149 Trieste, Italy*

ARTICLE INFO

Keywords:
Ion selection
Photoionization
Octupole ion guide
Merged-beam technique
Xe^+ ions
XUV spectroscopy

ABSTRACT

This paper describes the design and experimental validation of the OctoIonGuide, a compact setup for high-resolution photoionization studies of low-charge atomic ions with synchrotron radiation. The system integrates an axial ion source, a 40 cm RF octupole ion guide, and a quadrupole mass analyser, providing precise ion transport and mass selection. A proof-of-principle experiment on Xe^+ ions in the 20–22 eV range demonstrated the ability to resolve Rydberg resonances converging to the Xe^{2+}. The recorded spectra showed excellent agreement with reference data, confirming the accuracy and reliability of the setup. The novelty of this work lies in combining these components into a single, integrated platform, offering improved ion handling and compatibility with synchrotron and free-electron laser facilities. The OctoIonGuide represents a versatile tool for studying ionization dynamics relevant to laboratory astrophysics and plasma physics.

1. Introduction

The study of matter in its ionic state represents a formidable experimental challenge, particularly when dealing with atomic ions [1]. Ionic photoionization occurs in cosmic environments, motivating detailed laboratory studies of photon-ion interactions. However, these studies are challenging, as single-photon excitation of valence electrons requires radiation in the vacuum ultraviolet (VUV) and extreme ultraviolet (EUV) spectral regions. Such environments include, for example, active galactic nuclei and stellar atmospheres, where intense radiation fields and high temperatures ionize the gas, producing plasmas spanning a wide range of charge states, including low-charge ions that are abundant in cooler or partially ionized regions [2–4]. At these wavelengths, individual photons possess enough energy to excite inner-shell electrons in low-atomic-number species or to access multi-electron and valence-shell photoionization processes in higher-atomic-number ions. Experimental studies play a crucial role in providing essential data for understanding atomic and ionic processes in both laboratory and astrophysical plasmas, as well as for validating advanced theoretical model [5]. In the past decade, there has been a significant rise in the number of absolute photoionization cross-section measurements of atomic ions. Several research teams have contributed to the production of a large database of ionization energies and cross sections of the photo-ionization processes of atoms and atomic ions by using experimental setups based on the merged beam technique [6–11], or ion traps such as the Electron Beam Ion Trap (EBIT) [12] coupled with ionizing radiation with wavelengths from the VUV to X-rays, produced by lasers, free electron lasers or synchrotron radiation [13]. Beyond merged-beam configurations, photon–ion crossed-beam geometries have been realized at advanced light-source facilities, notably at the FLASH free-electron laser in Hamburg. At FLASH, the PG2 beamline together with the TIFF interaction region provides a well-defined 90° photon-ion intersection, enabling the interaction of pulsed ion beams with intense XUV free-electron-laser radiation [14], and, more recently, at the ASTRID2 synchrotron in Aarhus, Denmark [15], where a dedicated electron–ion coincidence spectrometer enables absolute photon-intensity determination and beam diagnostics for atomic and molecular physics experiments. We further note that a key advantage of the merged-beams technique-used in Refs.6–11 is its capability to measure photoionization cross sections on an absolute scale, a feature that distinguishes it from typical crossed-

---

[*] Corresponding author.
E-mail address: awad.mohamed@unicam.it (A.E.A. Mohamed).

https://doi.org/10.1016/j.nimb.2026.166112
Received 28 October 2025; Received in revised form 23 March 2026; Accepted 30 March 2026

beam configurations. Previous investigations of the photoionization of low-charge atomic ions have predominantly employed freely propagating ion beams, without the use of an ion-guiding device in the photon–ion interaction region [16–18]. In this work, we present a compact guided-beam configuration designed for efficient transport of low-intensity ion beams at moderate kinetic energies within a laboratory-scale apparatus. This approach complements conventional large-scale merged-beam and trapped-ion experiments by enabling a reduced system size while maintaining controlled interaction conditions. The RF multipole provides continuous transverse confinement of the ion beam along the interaction region. It is important to emphasize that such confinement does not result in phase-space cooling or a reduction of intrinsic beam emittance in the absence of collisional damping [19]. Instead, the ion guide suppresses geometric beam expansion arising from the initial angular divergence, thereby reducing transmission losses and maintaining a stable spatial overlap between the ion beam and the photon field over the available interaction length. Different experimental platforms offer distinct advantages for photoionization studies of low-charge ions. In electron beam ion traps (EBITs), confinement is achieved through the combined electrostatic and magnetic fields associated with the electron beam, enabling studies of highly charged ions under well-defined conditions. In contrast, extracted ion-beam approaches provide continuous beam transport and allow for precisely defined interaction geometries [20]. Crossed- and merged-beam photoionization experiments are typically conducted at large-scale synchrotron or free-electron-laser facilities, where extensive beamline infrastructure supports high-energy operation and long interaction regions. The present work is motivated by the development of a compact and adaptable system capable of operating under laboratory-scale constraints while preserving efficient ion transport and stable photon–ion overlap. In this paper, we describe a compact and versatile system, based on the merged beam design, that we called OctoIonGuide (OIG) aimed at the production and analysis of low-charge atomic ions. This system was developed by upgrading the existing OctoMass setup [21,22]. The optimization of the setup focused on maximizing ion transmission efficiency and effective ion–photon interaction in the interaction region, while maintaining controlled ion beam energy, spatial distribution, and reliable mass selection. Additionally, the OIG setup is designed to be compact and easily transportable, making it suitable for use at various synchrotron and free-electron laser facilities.

Start to end simulations of the ion pathway along the various stages composing OIG were examined to optimize ion optics of the system and the set up was characterized by experimental tests of operation of its different stages. In particular, the experimental tests focused on the ion source and the efficiency of ion transport through all the components of the system, using noble gases such as Ne, Ar, Kr and Xe, whose ions were produced in different charge states.

A brief overview of the instrument is provided, along with a proof-of-principle measurement on the photoionization of outer-valence electrons of singly charged xenon, which constitutes the focus of the present study.

2. Experimental design

A schematic top view of the Octupole Ion Guide (OIG) system is provided in Fig. 1. The figure highlights its four key functional stages, which are described in detail below. The overall dimensions of the setup are 900 mm × 970 mm × 1620 mm, emphasizing the compactness and portability of the system.

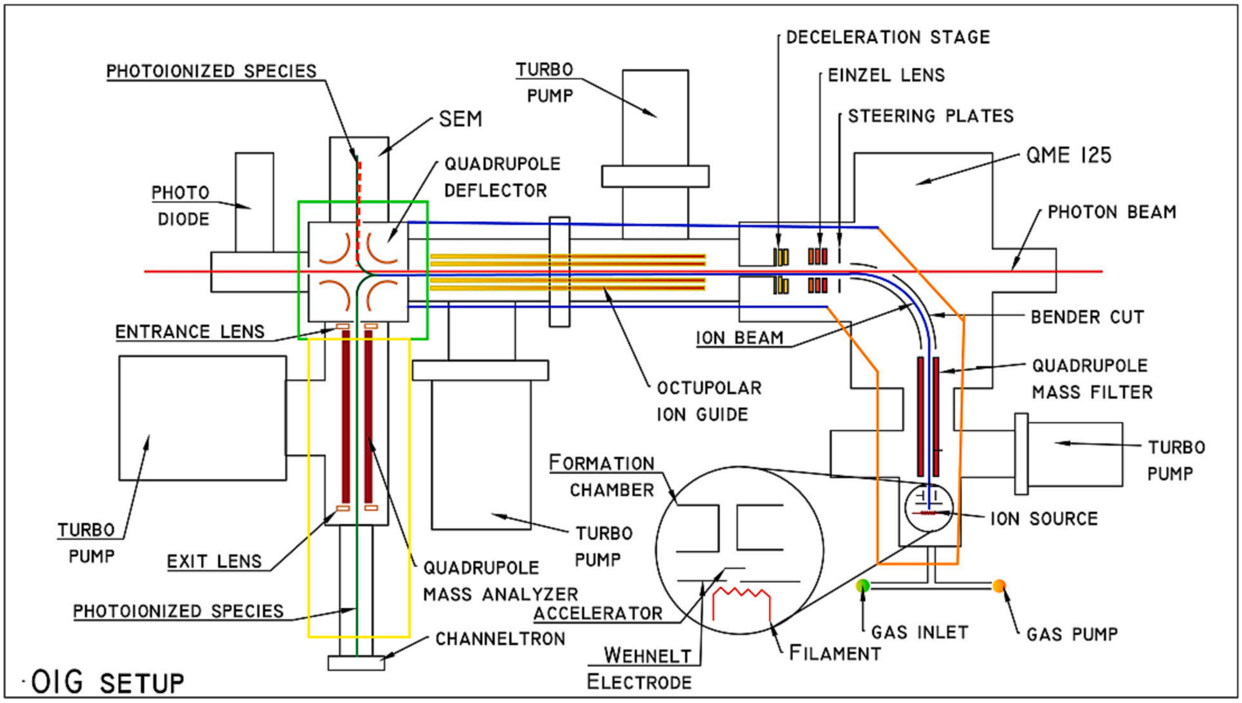

Fig. 1. Schematic diagram of the OctoIonGuide (OIG) setup. The system comprises several functional regions for ion generation, transport, and analysis, indicated by coloured zones: (1) the orange zone represents the atomic ion source; (2) the blue zone corresponds to the rectilinear ion transport region, where the ion beam propagates collinearly with the photon beam, enabling photoionization; (3 the green zone contains the quadrupole deflector. The solid ion trajectory indicates the operational beam path toward the ion analysis section, while the dashed red trajectory represents an alternative diagnostic path toward a secondary electron multiplier (SEM), used for beam alignment and verification before and after photoionization measurements. Only one trajectory is active at a time, depending on the applied deflector voltages. The photon beam transmitted through the interaction region exits the deflector and is detected downstream by a photodiode, allowing measurement of the photon flux after the interaction region; (4) the yellow zone is the ion analysis region, where the ionization products are characterized in terms of mass-to-charge ratio (m/q) and intensity.

2.1. The ion source

The ion source is a modified commercial ionizer Pfeiffer Vacuum (model: QMA 125) with axial geometry, that ensures good collimation of atomic ions entering the following mass filtering stage under high vacuum conditions. An electron currents up to 1 mA is accelerated toward the ionization chamber, which is kept at approximately 100 V. Electron collisions produce atomic ions by ionizing atomic gases (e.g., noble gases) or through ionization and dissociation of molecular gases (e.g., N_2, CO, O_2), producing a plasma [23–26]. The generated ions are extracted through an entry aperture at ground potential and directed to a quadrupole mass filter, consisting of four cylindrical rods, each with a length of 100 mm and a diameter of 6 mm, arranged with a field radius of 2.6 mm. The rods, made of stainless steel, are precisely aligned to ensure optimal performance in mass separation. An adjustable radio-frequency (RF) voltage, combined with a superimposed direct current (DC) voltage, is applied to the rod system to create the required electric field for ion trajectory control. The ion trajectories within the electric field are determined by their mass-to-charge (m/q) ratio [27]. The field allows only ions with a specific m/q ratio to maintain stable trajectories and pass through the filter, while all other ions are deflected and excluded. This selective filtering mechanism ensures high-precision mass separation and contributes to the accuracy and reliability of the experimental setup [28]. The quadrupole mass filter (QMF) at the ion source provides a constant mass resolution of $\geq$0.3 u, which can be adjusted via the applied RF and DC voltages. The typical ion-beam intensity for krypton (Kr) at a source pressure of 4.9×10^{-6} mbar was measured to be ~9 nA on a Faraday cup positioned in front of the quadrupole analyzer, corresponding to a flux of $\sim 5.6 \times 10^{10}$ ions/s, including contribution from all krypton charge states and residual background ions. Extracted ions have a nominal kinetic energy of 300 eV per unit charge (300 eV for Kr^+) after the bender cut, which is subsequently modified by deceleration and focusing stages before entering the octupole ion guide. The beam-energy spread was measured using a Faraday cup with a retarding potential scan and is approximately σ_exp ≈ 1.44 V; a detailed discussion and comparison with simulations is provided in Section 3.2.

2.2. Ion transport

The mass-selected ion source stage is based on a modified commercial QMA 125 system (Pfeiffer^{TM}), which includes a deviating unit. The bender cut (deviating unit) of the QMA 125 has been custom-drilled through its back surface to allow the photon beam to pass directly toward the octupole. This modification enables effective overlap and interaction between the photon beam and the ion beam within the interaction region. After passing through the deviating unit, the mass-selected ions are injected into an octupole ion guide, which defines the interaction region. The octupole ion guide is 40 cm in length and consists of eight rods arranged symmetrically with an inner diameter of 1 cm. Each rod has a diameter of 1 mm. The device operates at a radio-frequency (RF) of 6 MHz with a peak-to-peak voltage amplitude of 175 V.

2.3. Separation of photons and photo-ions

In the third stage of the OIG, the ion-photon separation is achieved using an electrostatic quadrupole deflector that bends the ion beam toward a final mass analyser. The deflector features a central opening that permits the transmitted photon beam to continue along its path to a photodiode, enabling simultaneous monitoring of the photon intensity after the interaction with the ions.

2.4. Analysis of the products

The final analysis of the photoionized species generated through ion–photon interactions is performed using a high-resolution, wide-mass-range quadrupole mass analyzer (Extrel®), capable of detecting ions up to 3000 amu. The analyzer employs four electrically isolated rods configured to produce a hyperbolic electric field for mass filtering, with entrance and exit ion optics optimizing ion transmission [29]. Mass-selected ions are guided along the central axis by combined DC and RF fields. The quadrupole mass analyzer features an actively adjustable mass resolution controlled via the ΔRes input (±5 V), which modifies the RF/DC ratio; positive ΔRes values yield narrower mass peaks at the expense of transmission, while negative values broaden the peaks. For the present experiments, ΔRes was optimized prior to data acquisition to ensure reliable separation of the selected ion species. At the quadrupole's output, a channel electron multiplier operated at negative high voltage efficiently collects the positively charged ions, and the resulting signals are processed through a preamplifier to ensure sensitive and accurate detection [30–32].

3. Ion trajectory simulation through OIG components

In the following, we detail the ion beam trajectories through the bender cut, the electrostatic lens system, and the quadrupole deflector, as evaluated using the Ion and Electron Optics Simulator (SIMION®). These simulations were performed using the actual geometries implemented in the instrument, with fixed ion mass and charge values. The primary goal was to identify the optimal electrode potentials that maximize transmission efficiency and overall instrument brightness while maintaining the energy resolution of the photoionization spectra. The kinetic energy distribution of the ion beam emerging from the electrostatic lens was also simulated and benchmarked against experimental data acquired using a Faraday cup positioned downstream of a retarding mesh.

3.1. Bender cut

The bender cut functions as a key ion deflection component that enables photon–ion interaction within the experimental setup. To evaluate its performance, the electrostatic field distribution was modelled using the SIMION® code (version 8.2.0.5) by solving the Laplace equation for the relevant geometry (Fig. 2). Ion trajectories were simulated for Ar^+ ions (mass 40 amu) after mass selection in the first QMA. Inside the QMA, ions have a kinetic energy of a few electron volts to ensure proper mass separation. Following the bender cut, the ions are

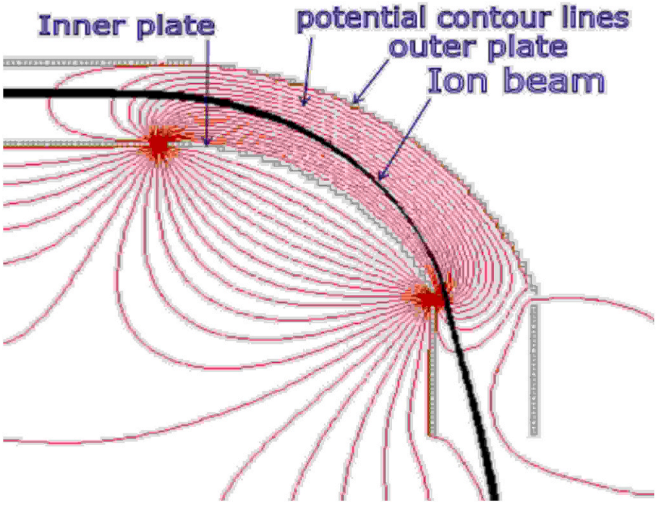

Fig. 2. SIMION® ion beam simulation trajectories for Ar^+ ions through the bender cut, where the outer plate is kept at ground potential while a negative potential is applied, to the inner plate ensuring that the ion beam bends by 90 degrees.

accelerated to 300 eV, and this post-acceleration energy was used as the initial condition for the trajectory simulations. The outer electrode of the ion bender was maintained at ground potential, while the inner electrode was biased at −270 V. A beam correction plate located at the bender entrance was differentially biased at +25 V and −25 V to allow fine-tuning of ion trajectories. Ion transmission was evaluated as a function of the inner electrode potential. The simulation results reveal a well-defined operational voltage range between approximately −280 V and −210 V, within which nearly full ion transmission is achieved. Outside this range, transmission drops sharply, indicating the inability of the bender to provide the required net beam redirection.

3.2. The electrostatic lens

We have developed a custom ion optics assembly (Fig. 3) for precise focusing and deceleration of ions prior to their injection into the octupole stage. To enhance beam alignment, two correction plates (element 10 in Fig. 3), biased at 0 V and –20 V, were incorporated. Beam focusing is performed using an Einzel lens (element 3 in Fig. 3), featuring a central electrode with a 14 mm aperture and an applied potential of –255 V. This is followed by a deceleration stage (element 8 in Fig. 3), consisting of a 15 mm aperture and a +105 V bias, which enables control over the kinetic energy of the ions before they enter the interaction region [33]. The simulations assume a nominal Ar^+ beam energy of 150 eV with an idealized, narrow initial energy spread, whereas the experimentally observed energy distribution includes additional broadening arising from the ion source, angular divergence, and transport through electrostatic elements.

Ion trajectories through the electrostatic lens system were simulated for Ar^+ ions to evaluate beam dynamics. As shown in Fig. 3 and Fig. 4, the ions are first corrected by the steering plates, then focused by the Einzel lens, and finally decelerated before reaching the octupole. The ion trajectories shown in Fig. 4 are initialized at the exit of the upstream optics with a finite angular deviation, resulting in beam steering at the intermediate focal plane, which is corrected by the downstream ion-optical elements. To assess the energy distribution, a virtual planar retarding potential was applied upstream of the octupole and the transmitted ion fraction was evaluated as a function of the retarding voltage. Fig. 5 shows the overlay of simulated and experimental ion transmission curves as a function of the splat/deceleration potential. Both datasets were fitted using an error function, corresponding to the cumulative distribution function (CDF) of a Gaussian energy distribution. The derivatives of these smooth fits yield the corresponding Gaussian energy profiles (inset), providing well-defined mean energies and widths. The mean ion energies are close to 150 V in both cases, with an energy spread of $\sigma\_exp = 1.437 \pm 0.100$ V for the experiment and $\sigma\_sim = 0.654 \pm 0.007$ V for the simulation. The slightly broader experimental distribution arises from instrumental broadening and other experimental effects. By presenting both curves in a single panel, a direct comparison between simulation and experiment is facilitated, highlighting the agreement in cutoff voltage and the difference in energy spread.

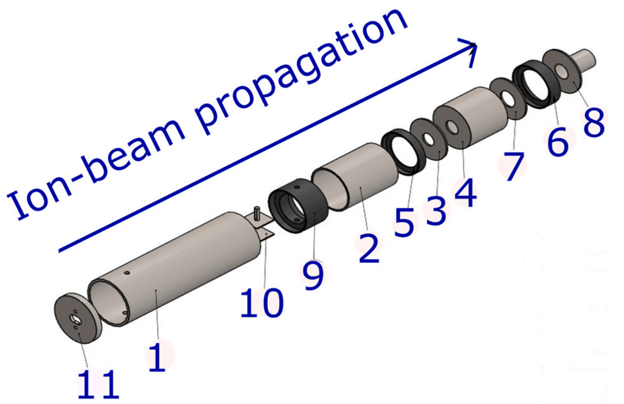

Fig. 3. A simplified CAD design of the electrostatic lenses is provided, along with a detailed description of all their components. 1- guard cylinder 2-guard cylinder 3- Einzel lens 4- guard cylinder 5- peek 6- peek 7- Deceleration lens 8- Deceleration lens injection element 9- peek 10- Horizontal steering plate 11- Quadrupole exit. The ion-beam propagation direction is indicated by the arrow. The CAD drawing is not to scale.

3.3. Quadrupole deflector

A quadrupole deflector (QD) with a compact cubic geometry (65 mm side length) is mounted at the exit of the octupole ion guide to decouple the trajectories of charged particles and the photon beam. The internal structure consists of four quarter cylindrical electrodes (length: 63 mm, radius: 28 mm) arranged symmetrically to face one another within a cubic enclosure formed by six planar surfaces. This configuration enables electrostatic deflection of the ion beam. The central aperture of the deflector has a diameter of 7 mm.

By applying controlled potentials to the cylindrical rods and surrounding surfaces, the ion beam can be steered by 90° to the left, as illustrated in Fig. 6. Reversing the polarity of the applied voltages results in deflection by 90° to the right. This bidirectional control is particularly advantageous for preliminary ion beam alignment, either via a Faraday cup or a secondary electron multiplier (SEM) detector located opposite to the quadrupole mass analyser entrance. Once aligned and maximised the signal, the ion beam can be redirected toward the quadrupole mass analyser to detect photoionized products resulting from photon-ion interactions. Moreover, this deflection scheme provides a diagnostic checkpoint for the ion beam before and after the photoionization interaction. Depending on the applied quadrupole deflector voltages, the ion beam can be directed either toward the ion analysis section or toward a secondary electron multiplier (SEM) for beam diagnostics. Only one deflection path is used at a time. The photon beam transmitted through the interaction region is detected downstream, enabling measurement of the photon flux after the interaction, which is required for normalization in the determination of absorption cross sections.”

To characterize the energy dispersion of the mass-selected Ar^+ or Ar^{2+} ion beam at the QD exit, the transmission efficiency was measured as a function of the voltages V1 and V5, which are responsible for the deflection of the ion beam. Here, V1 and V5 are the voltages applied to the opposing exit electrodes of the quadrupole deflector; in Fig. 7, the voltage of V1 is scanned while V5 is set to the same magnitude with opposite polarity. As shown in Fig. 7, the SIMION data (blue dots) were fitted with super-Gaussian fit (red line), defined as a Gaussian profile with an adjustable exponent. This functional form was chosen for its flexibility in describing the effective transmission window and for providing a robust estimate of the voltage range over which efficient transmission is maintained, rather than for a detailed physical modelling of the distribution. Maximum transmission (≈100% relative transmission) occurs at ∼130 V, with a full width at half maximum (FWHM) of approximately 20 V, indicating the energy range over which efficient transmission is maintained. The plateau observed at the top of the transmission curve indicates that the majority of ions are successfully guided through the exit aperture. Within this optimized voltage range, small variations in the deflector potential do not significantly alter the ion trajectories, resulting in a nearly constant transmission efficiency. This result emphasizes the sensitivity of the beam transport to voltage settings and provides an optimized window for ion manipulation.

4. Experimental evaluation of OIG transmission efficiency

To evaluate the transmission characteristics of the ion transport system, a series of measurements were performed using singly and doubly charged argon ions (Ar^+ and Ar^{2+}). The ions were extracted from the ion source, passed through the bender cut and electrostatic lenses,

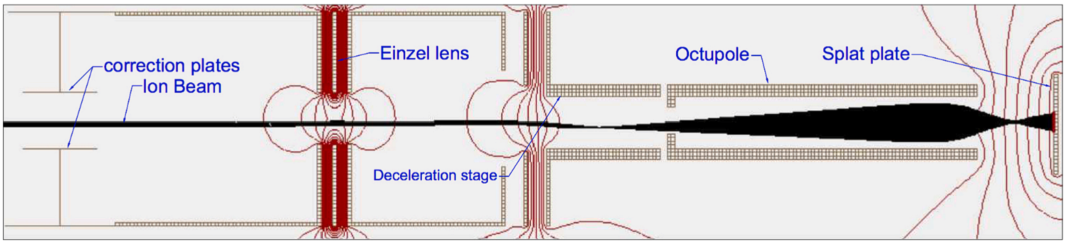

Fig. 4. SIMION® model of the electrostatic lens simulated for focus and decelerating ions, using two deflecting plate, focusing and deacceleration stages as shown in the CAD design Fig. 3.

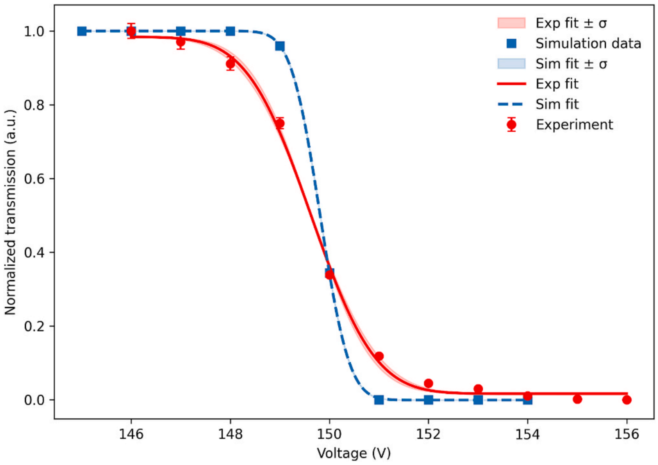

Fig. 5. Experimental (red circles) and simulated (blue squares) ion transmission as a function of deceleration voltage, with error-function fits (solid red and dashed blue lines). Shaded areas indicate the fit uncertainties (±σ). The derivative of the fitted curves yields the corresponding Gaussian energy distributions (inset), showing a peak near 150 V. The experimental energy spread is σ_exp = 1.437 ± 0.100 V, and the simulated energy spread is σ_sim = 0.654 ± 0.007 V.

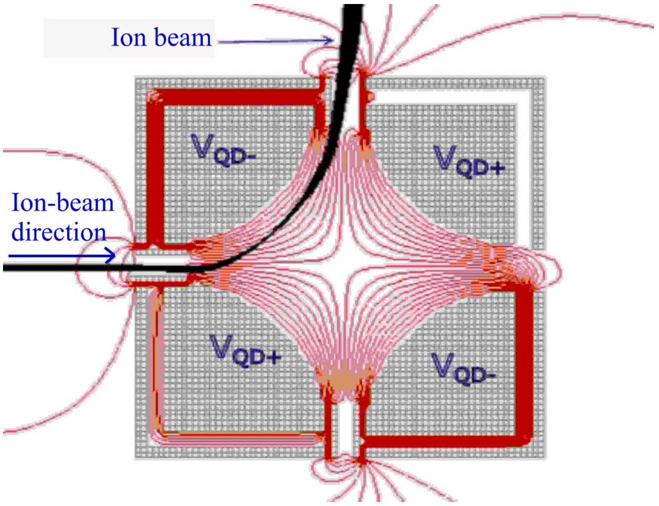

Fig. 6. SIMION® model of the quadrupole deflector. The figure illustrates the simulated trajectories of Ar^{+} ions (250 trajectories shown in black). The simulation provides the paths followed by the ions under the influence of the specified electric potentials and electric field. The ion-beam propagation direction is indicated by the blue arrow.

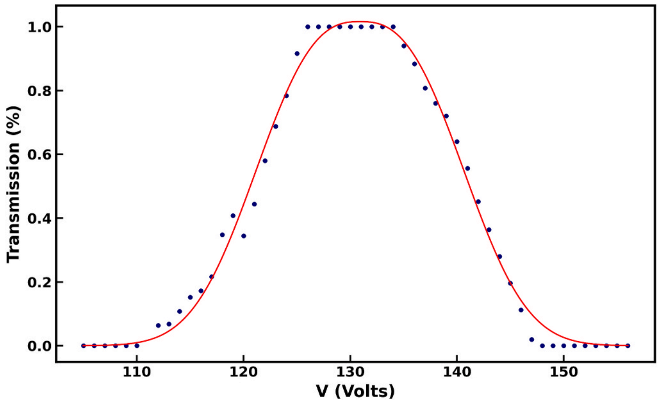

Fig. 7. Transmission characteristics from the ion source to the detection system. The blue data points correspond to SIMION®-simulated the transmission as a function of the exit potentials of the QD. The data were fitted with a super-Gaussian function, resulting in a full width at half maximum (FWHM) of about 20 V.

and transported through the octupole ion guide before reaching the quadrupole deflector. All ion-current and transmission measurements discussed below were performed downstream of the octupole ion guide. Ion currents were measured either with all quadrupole deflector electrode voltages set to 0 V or with deflection voltages applied to steer the beam toward the right-hand exit. Measurements were performed sequentially using a Faraday cup and a secondary electron multiplier (SEM), enabling a direct comparison of ion transport and detection efficiency under identical beam and pressure conditions.

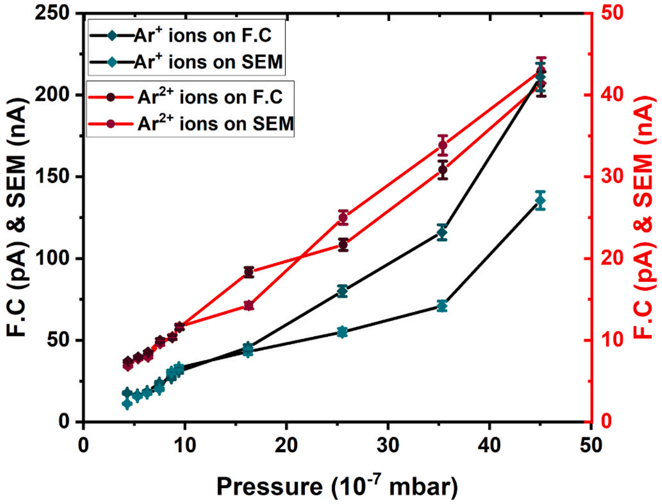

Fig. 8. The ion yield of Ar^{+} and Ar^{2+} detected using a Faraday cup and SEM, both before and after deflection, as a function of the pressure. The plot illustrates the variation in ion yield with changes in pressure, highlighting the differences in detection methods and the impact of the deflection process on the ion signal.

Fig. 8 shows the detected ion current as a function of source pressure for Ar^{+} and Ar^{2+} ions measured with both detectors. As expected, the ion current increases with pressure due to enhanced ion production at higher gas densities. The Ar^{2+} signals exhibit a steeper pressure dependence than the Ar^{+} signals, indicating more efficient formation of doubly charged ions at elevated pressures. Within experimental uncertainties, the pressure-dependent trends measured by the Faraday cup and SEM are consistent, providing cross-validation between the two detection methods.

The inclusion of statistical uncertainties, derived from ion counting statistics, allows a quantitative assessment of these trends. For both charge states, the increase in ion current with pressure significantly exceeds the associated uncertainties, confirming that the observed pressure dependence is statistically meaningful. Although the absolute uncertainties increase at higher pressures due to larger ion currents, the relative uncertainties remain approximately constant, indicating stable ion transport and detection conditions throughout the investigated pressure range.

Fig. 9 presents the corresponding percentage transmission of Ar^{+} and Ar^{2+} ions from the ionization source to the quadrupole deflector as a function of pressure in the range of approximately 10^{-7} mbar. At low pressures, the transmission of both charge states remains constant within experimental uncertainties, demonstrating stable ion transport under high-vacuum conditions. The Ar^{2+} transmission generally exceeds that of Ar^{+}; however, point-to-point variations at low pressure are comparable to the statistical uncertainties and are therefore not interpreted as systematic trends. At intermediate and higher pressures, deviations exceeding the error bars are observed, suggesting pressure-dependent effects that may arise from space-charge interactions or pressure-induced changes in ion focusing and transport efficiency.

These results collectively suggest that the ion transmission efficiency depends on both the ion charge state and the background pressure. In the investigated pressure range, doubly charged ions consistently exhibit higher transmission than singly charged ions, which may be attributed to stronger electrostatic confinement and a reduced sensitivity to small trajectory perturbations. Furthermore, the consistent pressure-dependent behaviour observed in both the transmission measurements and the detected ion currents indicates stable and reproducible ion delivery to the mass spectrometer, which is essential for reliable spectroscopic measurements.

5. Mass spectral analysis and selection of individual ion species

To characterize the ion source output and the transmission through the complete OctoIonGuide (OIG) setup, mass spectral analysis of atomic ions generated from noble gases was performed. Noble gas was injected into the source, and both the quadrupole mass filter at the source and the downstream mass analyzer were scanned simultaneously using identical mass settings, ensuring that only ions transmitted through the full OIG setup were detected. Fig. 10 presents the resulting charge-state distribution of krypton (Kr) ions extracted from the plasma, transmitted through the full setup, and detected with the channeltron. The data show that krypton ions were successfully ionized up to the $Kr4^{+}$ charge state, demonstrating the ion source's effectiveness in producing multiply charged species.

In addition to Kr ions, the mass spectrum also revealed the presence of background ions such as N_2^{+} and O_2^{+}, originating from residual gas in the vacuum chamber. To further validate system performance, similar measurements were performed using argon (Ar) and xenon (Xe). In all cases, the ion source consistently produced low charge state ions with good signal-to-noise ratio, confirming its suitability for a range of atomic species.

A key aspect of this setup is its ability to select specific charge states with high precision. The combination of ion optics and the quadrupole mass filter enables effective separation of the target ion species from background contaminants. As shown in Fig. 11, the measured spectra demonstrate the high selectivity of the system toward mass-selected ions. For these measurements, the upstream quadrupole mass filter was pre-set to transmit a selected parent-ion mass-to-charge ratio, while the downstream quadrupole mass analyzer was scanned to resolve the charge-state distribution. Prior to scanning the photon energy for the photoionization, mass selection was therefore performed to ensure that only the desired ion species were targeted. Although Ar^{+} and Kr^{2+} have similar m/q ratios, the Ar^{+} peak is narrower due to its smaller energy spread and lower sensitivity to ion-optical aberrations compared to multiply charged ions. The resulting spectra clearly show signals corresponding solely to the selected ions, confirming the system's strong background suppression capability. It should be noted that the objective of this measurement was not to assess spectral resolution, but rather to verify the overall transmission performance of the OIG setup.

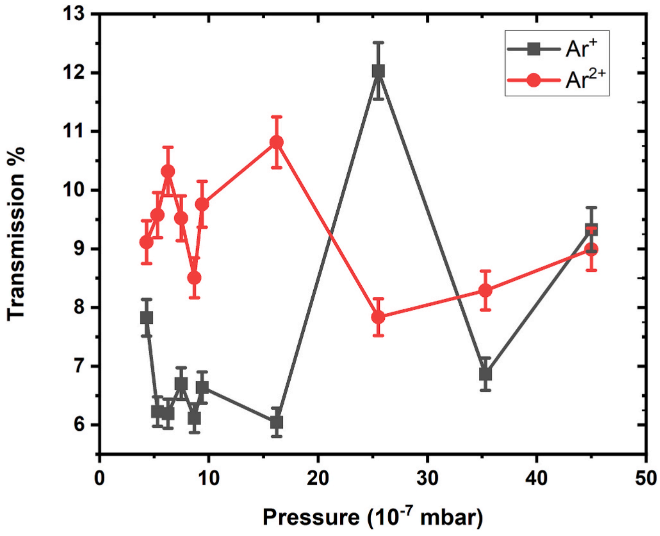

Fig. 9. Ion yield of Ar^{+} and Ar^{2+} as a function of pressure, expressed as the percentage transmission from the ionization source to the quadrupole deflector under high-vacuum conditions. Error bars represent one standard deviation derived from ion counting statistics.

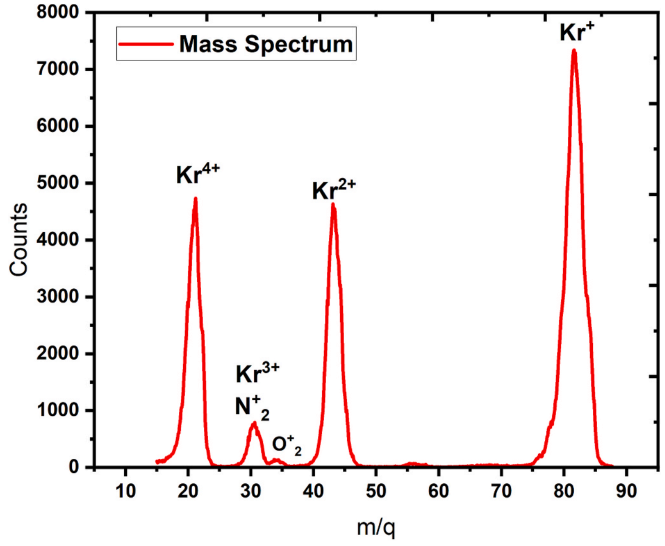

Fig. 10. Mass spectrum of ionized krypton gas generated in the QMA ion source, guided through the OctoIonGuide, and detected by the channeltron. The spectrum reveals the distribution of krypton-ionized species, demonstrating the system's ability to resolve and detect ions with high precision and reliability.

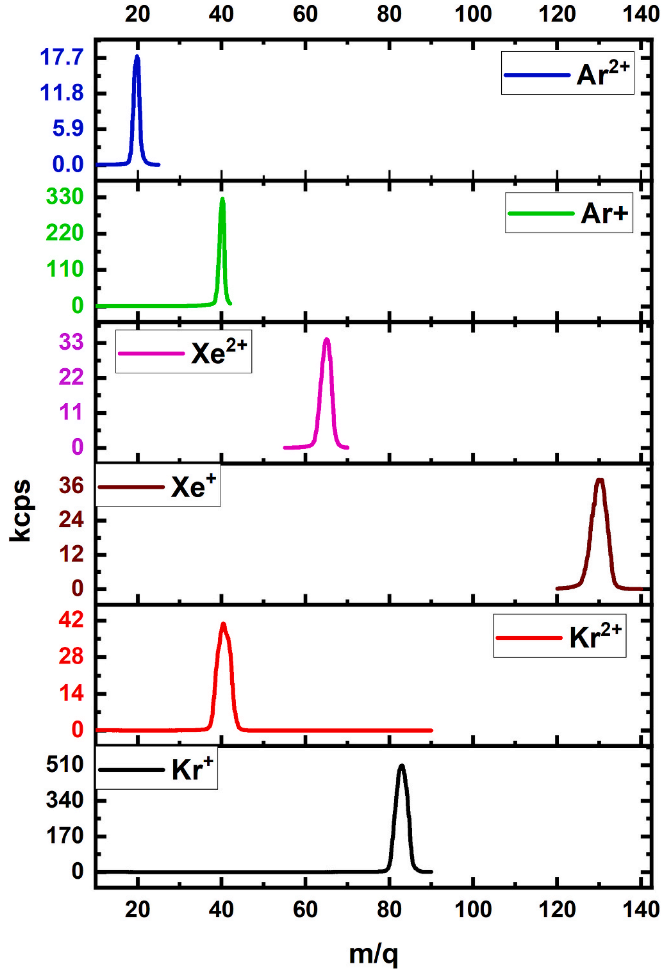

Fig. 11. Ion mass spectrum from the QMA ion source, displaying selected species such as Kr^+, Kr^{2+}, Xe^+, Xe^{2+}, Ar^+, and Ar^{2+}. The spectrum demonstrates the successful removal of background signals.

6. Experimental validation of the OIG setup with synchrotron radiation

Synchrotron radiation measurement were performed at the MOST@CiPo beamline of the Elettra Synchrotron facility (Trieste, Italy) [34], aiming to validate the performance of the proposed (OIG) setup. The MOST@CiPo beamline represents an upgrade of the original Circular Polarization beamline (CiPo) [35], which operated at Elettra until 2023, where the original elliptical wiggler source of CiPo has been substituted with the two novel insertion devices of the Molecular Science and Technology (MOST) beamline foreseen in the Elettra 2.0 upgrade program of the Italian National synchrotron radiation laboratory [34]. The main target of MOST@CiPo in the last year of operation of Elettra has been a preliminary commissioning of the new insertion devices (ID) sources, exploiting the CiPo optical layout. But the beamline has also been exploited to perform experimental upgrades in view of the scientific program of Elettra 2.0, such as the development of this new end station for photoionization studies of low-charge atomic ions for laboratory astrophysics.

Photoionization of Xe^+ ions was investigated over the photon energy range of 20 to 22 eV. The measured spectrum (Fig. 12) reproduces the positions of several dominant resonance features reported previously in this energy range [6,31]. This qualitative agreement in resonance positions supports the correct photon-energy calibration and demonstrates the reliable operation of the OIG configuration under merged-beam conditions.

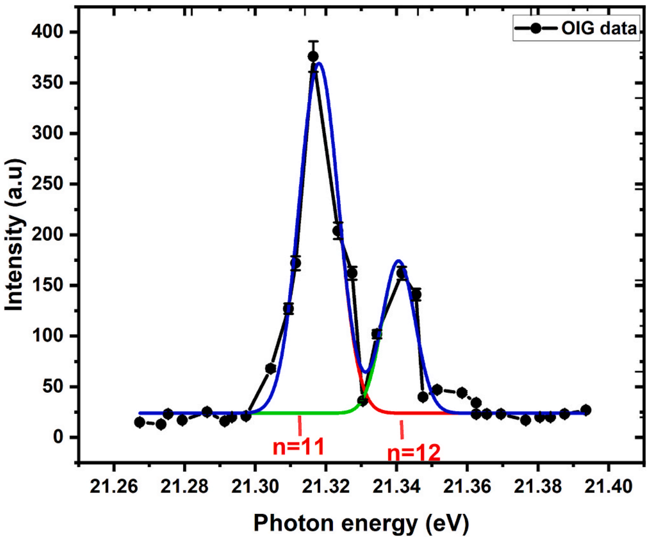

Fig. 12. Xe^{2+} photoionization yield recorded as a function of photon energy using the OIG setup. The spectrum is shown over a limited energy range as a proof-of-principle measurement. Two dominant resonance features are observed and are tentatively assigned to the n = 11 and n = 12 members of the $5s^25p^4(^1D_2)$ and Rydberg series of Xe^+ based on comparison with literature data [36].

The experimental conditions were carefully controlled to optimize ion production and measurement precision. The base pressure in the vacuum chamber was maintained at approximately 6×10^{-8} mbar. Xenon gas was introduced at pressures between 6×10^{-6} and 1×10^{-5} mbar into the ionization region to generate Xe^+ ions via electron impact ionization from a tungsten hot filament. Concurrently, neutral xenon gas was fed into a gas cell located upstream of the OIG at a pressure of 7×10^{-7} mbar to enable photon energy calibration.

Photon energy calibration was performed in real time by monitoring resonant absorption features of neutral xenon, specifically targeting the $5s^25p^6\ ^1S_0 \rightarrow 5s5p^6\ (^2S_{1/2})$ np electronic transitions [35]. An electron multiplier was positioned inside the experimental chamber, directly in front of the ionization region. The incident photon flux was measured contemporaneously using a calibrated silicon photodiode (AxVU100IRD) (see Fig. 1), which was used for spectral normalization. The absorption energy scale of Xe^+ was calibrated by recording reference absorption spectra of neutral Xe introduced into the ionization region under identical conditions.

The Xe^+ ions generated in the source were extracted and accelerated towards a mass filter that selectively transmitted ions based on their mass-to-charge ratio, as illustrated in Fig. 11. For the proof-of-principle measurement, the first QMF (ion source) was set to select Xe^+, while the second QMF (analyzer) was set to detect Xe^{2+}. After mass selection, the ions were deflected by 90°, focused, and decelerated before entering the 40 cm long octupole interaction region. Within this region, the ion beam (measured at approximately 1.3 nA using a Faraday cup before installing the octupole ion guide, corresponding to a flux of 8.11×10^9 ions/s, for the singly ionized Xenon) was merged with the synchrotron photon beam, enabling photoionization interactions. Resulting photoions were separated from the primary beam using a 90° quadrupole electrostatic deflector and subsequently focused through entrance and exit electrostatic lenses into a quadrupole mass analyser for further species selection. Detection was performed using a channeltron detector optimized for positive ions.

A photoionization spectrum of Xe^+ was recorded as a function of photon energy by scanning the Normal Incidence Monochromator of the beamline [34,35]. The entrance and exit slit widths were set to 50 μm, corresponding to an overall photon-energy resolution of approximately 11 meV. The photon energy was scanned using a step size of 2.5 meV with a dwell time of 2 s per point. While the full spectral range was explored during the experiment, the discussion presented here focuses on a selected energy interval containing a resonance feature, which is used as a proof-of-principle to benchmark the performance of the OIG setup for photoionization measurements.

The photon-energy scale was referenced using the absorption spectrum of neutral xenon recorded in an upstream gas cell. Several well-resolved resonances associated with the $5s^25p^6\ ^1S_0 \rightarrow 5s5p^6\ (^2S_{1/2})$ transitions were identified and used as internal reference points. Gaussian fits to five prominent lines yielded measured peak positions that show a linear correlation with previously reported energies [36]. The resulting linear correction was applied to the Xe$^+$ photoionization data to establish a consistent photon-energy scale.

As a proof of principle, two resonances observed in the 21.26–21.4 eV region (Fig. 12) are consistent with excitation of the $5s^25p^4(^1D_2)nd$ Rydberg series of Xe$^+$. Comparison with previously reported resonance energies [37] allows the two strongest features to be assigned to the n = 11 and n = 12 members of the series. The observed resonance positions agree with literature values within the experimental resolution of the present setup, confirming the correct operation of the OIG configuration.

7. Conclusion

In this work, we developed and validated a compact and transportable octupole ion guide (OIG) system designed for photoionization studies of atomic ions. The setup integrates a quadrupole mass analyser, a 40 cm octupole interaction region, a quadrupole electrostatic deflector, and mass-filtering capabilities, enabling precise ion selection, transport, and detection under controlled experimental conditions.

As a proof-of-principle measurement, the photoionization spectrum of Xe$^+$ ions were measured over the photon energy range of 20–22 eV using synchrotron radiation at the MOST@CiPo beamline of Elettra.

The OIG setup offers a flexible and portable solution for advanced ion–photon interaction experiments, compatible with synchrotron and free-electron laser (FEL) facilities. Future developments will focus on extending detection capabilities to lower atomic number species and implementing high resolution measurements of inner-shell ionization processes with the goal of determining absolute cross section.

CRediT authorship contribution statement

Awad E.A. Mohamed: Writing – review & editing, Writing – original draft, Visualization, Validation, Software, Resources, Methodology, Investigation, Funding acquisition, Formal analysis, Data curation, Conceptualization. **Marcello Coreno:** Writing – review & editing, Validation, Supervision, Resources, Project administration, Methodology, Investigation, Funding acquisition, Formal analysis, Data curation, Conceptualization. **Daniele Catone:** Writing – review & editing, Supervision, Resources, Methodology, Funding acquisition, Conceptualization. **Fabio Zuccaro:** Validation, Resources, Methodology, Investigation, Data curation. **Stefano Orlando:** Writing – review & editing, Investigation, Data curation. **Javad Rezvani:** Writing – review & editing, Supervision, Funding acquisition. **Andrea Di Cicco:** Writing – review & editing, Supervision, Funding acquisition. **Monica de Simone:** Validation, Supervision, Resources, Methodology, Investigation, Funding acquisition, Formal analysis, Data curation.

Funding

The authors acknowledge the support of the AHEAD2020 project for high-energy astrophysics under grant No. 871158, as well as the funding provided by the TRIL Program of the Abdus Salam International Centre for Theoretical Physics (ICTP). A. E. A. Mohamed gratefully acknowledges financial support from the University of Camerino and CNR-ISM for his PhD grant. M. Coreno, D. Catone and F. Zuccaro acknowledge funding from EUROFEL-ROADMAP ESFRI of the Italian Ministry of University and Research.

Declaration of competing interest

The authors declare the following financial interests/personal relationships which may be considered as potential competing interests: Awad Elamin Awad Mohamed reports financial support was provided by University of Camerino. Awad Elamin Awad Mohammed reports a relationship with AHEAD2020 project for high-energy astrophysics that includes: funding grants. Awad Elamin Awad Mohammed reports a relationship with the TRIL Program of the Abdus Salam International Centre for Theoretical Physics (ICTP) that includes: funding grants. Awad Elamin Awad Mohamed reports a relationship with University of Camerino and CNR-ISM that includes: funding grants. M. Coreno, D. Catone and F. Zuccaro reports a relationship with from EUROFEL-ROADMAP ESFRI of the Italian Ministry of University and Research. that includes: funding grants. If there are other authors, they declare that they have no known competing financial interests or personal relationships that could have appeared to influence the work reported in this paper.

Acknowledgments

The authors acknowledge the fundamental technical support received from dr. Robert Richter (Elettra, Trieste) in the development of this experimental setup. Sadly, dr. Robert Richter passed away while we were writing the manuscript, which we thus dedicate to his memory. This work received partial financial support by the LASYF project of Elettra Sincrotrone Trieste, Italy.

Data availability

Data will be made available on request.

References

[1] J.B. West, Photoionization of atomic ions, J. Phys. B: At. Mol. Opt. Phys. 34 (2001) R45–R91, https://doi.org/10.1088/0953-4075/34/18/201.

[2] J.H. Krolik, Active Galactic Nuclei: From the Central Black Hole to the Galactic Environment, Princeton University Press, Princeton, NJ, 1999.

[3] H. Netzer, The Physics and Evolution of Active Galactic Nuclei, Cambridge University Press, Cambridge, 2013.

[4] S. Schippers, A.L.D. Kilcoyne, R.A. Phaneuf, A. Müller, Photoionisation of ions with synchrotron radiation: from ions in space to atoms in cages, Contemp. Phys. 57 (2016) 215–229, https://doi.org/10.1080/00107514.2015.1109771.

[5] E.T. Kennedy, J.T. Costello, J.-P. Mosnier, P. Van Kampen, VUV/EUV ionising radiation and atoms and ions: dual laser plasma investigations, Radiat. Phys. Chem. 70 (2004) 291–321, https://doi.org/10.1016/j.radphyschem.2003.12.018.

[6] J.-M. Bizau, C. Blancard, M. Coreno, D. Cubaynes, C. Dehon, N. El Hassan, F. Folkmann, M.F. Gharaibeh, A. Giuliani, J. Lemaire, A.R. Milosavljević, C. Nicolas, R. Thissen, Photoionization study of Kr+ and Xe+ ions with the combined use of a merged-beam set-up and an ion trap, J. Phys. B: At. Mol. Opt. Phys. 44 (2011) 055205, https://doi.org/10.1088/0953-4075/44/5/055205.

[7] S. Schippers, S. Ricz, T. Buhr, A. Borovik, J. Hellhund, K. Holste, K. Huber, H.-J. Schäfer, D. Schury, S. Klumpp, K. Mertens, M. Martins, R. Flesch, G. Ulrich, E. Rühl, T. Jahnke, J. Lower, D. Metz, L.P.H. Schmidt, M. Schöffler, J.B. Williams, L. Glaser, F. Scholz, J. Seltmann, J. Viefhaus, A. Dorn, A. Wolf, J. Ullrich, A. Müller, Absolute cross sections for photoionization of Xe q+ ions ($1 \leq q \leq 5$) at the 3d ionization threshold, J. Phys. B: At. Mol. Opt. Phys. 47 (2014) 115602, https://doi.org/10.1088/0953-4075/47/11/115602.

[8] H. Kjeldsen, Photoionization cross sections of atomic ions from merged-beam experiments, J. Phys. B: At. Mol. Opt. Phys. 39 (2006) R325–R377, https://doi.org/10.1088/0953-4075/39/21/R01.

[9] H. Kjeldsen, F. Folkmann, J. van Elp, H. Knudsen, J.B. West, T. Andersen, Absolute measurements of photoionization cross-sections for ions, Nucl. Instrum. Methods Phys. Res. B 234 (2005) 349–361, https://doi.org/10.1016/j.nimb.2005.01.011.

[10] S. Reinwardt, I. Baev, F. Linß, P. Cieslik, O. Raberg, T. Buhr, A. Perry-Sassmannshausen, S. Schippers, A. Müller, F. Trinter, A. Guda, R. Laasch, M. Martins, An integrated ion trap for the photon–ion spectrometer at PETRA III, Rev. Sci. Instrum. 94 (2023) 023201, https://doi.org/10.1063/5.0111097.

[11] K. Hirsch, J.T. Lau, P.H. Klar, A. Langenberg, J. Probst, J. Rittmann, M. Vogel, V. Zamudio-Bayer, T. Möller, B. von Issendorff, X-ray spectroscopy on size-selected clusters in an ion trap: from the molecular limit to bulk properties, J. Phys. B: At.

Mol. Opt. Phys. 42 (2009) 154029, https://doi.org/10.1088/0953-4075/42/15/154029.

[12] P. Micke, S. Kühn, L. Buchauer, J.R. Harries, T.M. Bücking, K. Blaum, A. Cieluch, A. Egl, D. Hollain, S. Kraemer, T. Pfeifer, P.O. Schmidt, R.X. Schüssler, C. Schweiger, T. Stöhlker, S. Sturm, R.N. Wolf, S. Bernitt, J.R. Crespo López-Urrutia, The Heidelberg compact electron beam ion traps, Rev. Sci. Instrum. 89 (2018) 063109, https://doi.org/10.1063/1.5026961.

[13] A. Müller, Precision studies of deep-inner-shell photoabsorption by atomic ions, Phys. Scr. 90 (2015) 054004, https://doi.org/10.1088/0031-8949/90/5/054004.

[14] L.S. Harbo, A. Becker, S. Dziarzhytski, C. Domesle, N. Guerassimova, A. Wolf, H. B. Pedersen, Single and double electron photodetachment from the oxygen anion at 41.7 nm, Phys. Rev. A 86 (2012) 023409, https://doi.org/10.1103/PhysRevA.86.023409.

[15] H.B. Pedersen, S.J. Lanng, B. Bastian, L.S. Harbo, S.V. Hoffmann, N.C. Jones, M. Mudrich, T.A. Nielsen, A. Svendsen, R. Teiwes, An electron-ion coincidence spectrometer for commissioning of a synchrotron radiation beamline: absolute photon intensity and content of higher harmonic radiation, Rev. Sci. Instrum. 94 (2023) 053102, https://doi.org/10.1063/5.0147173.

[16] S. Schippers, A. Müller, Photoionization of astrophysically relevant atomic ions at PIPE, Atoms 8 (2020) 45, https://doi.org/10.3390/atoms8030045.

[17] K. Hirsch, V. Zamudio-Bayer, F. Ameseder, A. Langenberg, J. Rittmann, M. Vogel, T. Möller, B. von Issendorff, J.T. Lau, 2p X-ray absorption of free transition-metal cations across the 3d transition elements: calcium through copper, Phys. Rev. A 85 (2012) 062501, https://doi.org/10.1103/PhysRevA.85.062501.

[18] J.-P. Mosnier, E.T. Kennedy, D. Cubaynes, J.-M. Bizau, S. Guilbaud, C. Blancard, B. M. McLaughlin, M.F. Hasoğlu, T.W. Gorczyca, L-shell photoionisation cross sections in the S+, S2+, S3+ isonuclear sequence, J. Phys. B: At. Mol. Opt. Phys. 58 (2025) 075002, https://doi.org/10.1088/1361-6455/adb5e1.

[19] M. Martschini, J. Pitters, T. Moreau, P. Andersson, O. Forstner, D. Hanstorp, J. Lachner, Y. Liu, A. Priller, P. Steier, R. Golser, Selective laser photodetachment of intense atomic and molecular negative ion beams with the ILIAS RFQ ion beam cooler, Int. J. Mass Spectrom. 412 (2017) 73–79, https://doi.org/10.1016/j.ijms.2016.12.015.

[20] G.Y. Liang, J.R. Crespo López-Urrutia, T.M. Baumann, S.W. Epp, A. Gonchar, A. Lapierre, P.H. Mokler, M.C. Simon, H. Tawara, V. Mäckel, K. Yao, G. Zhao, Y. Zou, J. Ullrich, Experimental investigations of ion charge distributions, effective electron densities, and electron-ion cloud overlap in electron beam ion trap plasma using extreme-ultraviolet spectroscopy, Astrophys J 702 (2009) 838–850, https://doi.org/10.1088/0004-637X/702/2/838.

[21] D. Ascenzi, P. Tosi, P. Franceschi, D. Catone, S. Turchini, K.C. Prince, Chemical synthesis in acetonitrile containing discharges: insights from photoionization experiments with synchrotron radiation, Chem. Phys. 398 (2012) 269–277, https://doi.org/10.1016/j.chemphys.2011.06.009.

[22] D. Catone, M. Satta, M.C. Castrovilli, P. Bolognesi, L. Avaldi, A. Cartoni, Photoionization of methanol: a molecular source for the prebiotic chemistry, Chem. Phys. Lett. 771 (2021) 138467, https://doi.org/10.1016/j.cplett.2021.138467.

[23] W. Paul, H.P. Reinhard, U. von Zahn, Das elektrische Massenfilter als Massenspektrometer und Isotopentrenner, Z. Phys. 152 (1958) 143–182, https://doi.org/10.1007/BF01327353.

[24] Balzers AG, Partial pressure measurement in vacuum technology, BG 800 169 PE, Liechtenstein, 1983.

[25] Balzers AG, Gas tight ion source, Application Report BG 800 025 AE, Liechtenstein, 1989.

[26] D. Price (Ed.), Dynamic Mass Spectrometry, Vol. 2, Heyden & Son Ltd., London, 1971.

[27] P. Tosi, G. Fontana, S. Longano, D. Bassi, Transport of an ion beam through an octopole guide operating in the R.F.-only mode, Int. J. Mass Spectrom. Ion Process. 93 (1989) 95–105, https://doi.org/10.1016/0168-1176(89)83077-0.

[28] D. Gerlich, Inhomogeneous RF fields: a versatile tool for the study of processes with slow ions, in: C. Ng, M. Baer, I. Prigogine, S.A. Rice (Eds.), Advances in Chemical Physics, Wiley, 1992, pp. 1–176. Doi: 10.1002/9780470141397.ch1.

[29] R.E. Pedder, Practical quadrupole theory: graphical theory, Poster presented at the 49th ASMS Conference on Mass Spectrometry and Allied Topics, Chicago, IL, May 28–June 1, 2001.

[30] E. Teloy, D. Gerlich, Integral cross sections for ion–molecule reactions. I. The guided beam technique, Chem. Phys. 4 (1974) 417–427, https://doi.org/10.1016/0301-0104(74)85008-1.

[31] B.E. Wilcox, C.L. Hendrickson, A.G. Marshall, Improved ion extraction from a linear octopole ion trap: SIMION analysis and experimental demonstration, J. Am. Soc. Mass Spectrom. 13 (2002) 1304–1312, https://doi.org/10.1016/S1044-0305(02)00622-0.

[32] C. Hägg, I. Szabo, New ion-optical devices utilizing oscillatory electric fields. III. Stability of ion motion in a two-dimensional octopole field, Int. J. Mass Spectrom. Ion Process. 73 (1986) 277–294, https://doi.org/10.1016/0168-1176(86)80003-9.

[33] P.J. O'Connor, G.E. Leroi, J. Allison, Understanding ion deceleration lenses: what are the simplicity/performance trade-offs? J. Am. Soc. Mass Spectrom. 2 (1991) 322–335, https://doi.org/10.1016/1044-0305(91)80024-2.

[34] MOST beamline at Elettra 2.0, https://www.elettra.eu/lightsources/elettra-beamlines/most.html. (Accessed 2025).

[35] A. Derossi, F. Lama, M. Piacentini, T. Prosperi, N. Zema, High flux and high-resolution beamline for elliptically polarized radiation in the vacuum ultraviolet and soft X-ray regions, Rev. Sci. Instrum. 66 (1995) 1718–1720, https://doi.org/10.1063/1.1145828.

[36] K. Codling, R.P. Madden, The absorption spectra of krypton and xenon in the wavelength range 330–600 Å, J. Res. Natl. Bur. Stand. A 76 (1972) 1, https://doi.org/10.6028/jres.076A.001.

[37] B.M. McLaughlin, C.P. Ballance, Photoionization cross section calculations for the halogen-like ions Kr^+ and Xe^+, J. Phys. B: At. Mol. Opt. Phys. 45 (2012) 085701 https://doi.org/10.1088/0953-4075/45/8/085701.